Check for updates



ADVANCED FUNCTIONAL MATERIALS
www.afm-journal.de

# Fast Neutron Detector Based on Hybrid 2D Perovskite Thin Films

*Ilaria Fratelli, Felix Pino, Laura Basiricò,* Giulia Napolitano, Jessica Carolina Delgado, Sara Cepić, Andrea Ciavatti, Sandra Moretto, Gianluigi Maggioni, Marco Cinausero, Sara Maria Carturan,* and Beatrice Fraboni*

**2D hybrid perovskites are a novel and promising class of semiconductors for the realization of direct fast neutron detectors because they combine excellent transport properties with a large organic cation, rich in low-Z elements, which strongly interacts with fast neutrons. Here, this study presents the employment of $PEA_2PbBr_4$ ($PEA = C_6H_5C_2H_4NH_3^+$) thin films for the direct detection of fast neutrons. By tuning the perovskite deposition process, it achieves a stable and reproducible response capable to monitor in real-time the flux of fast neutrons (energy = [1–4] MeV; beam flux = [0.4–3] · $10^5$ n $s^{-1}cm^{-2}$) by providing an output electrical signal proportional to the radiation field intensity. Finally, the employment of a thin film-based device boosts the discrimination capability of this technology and offers the possibility to realize a flexible and easy-scalable detecting system very appealing for the development of wearable personal dosimeters.**

## 1. Introduction

The detection of fast neutrons is of great importance for several applications, including medical imaging, medical therapy, and non-destructive inspections. This kind of detection presents a significant challenge because of the small cross-section of interaction between fast neutrons and matter, due to neutrons charge neutrality. In essence, the primary mechanism for detecting fast neutrons, using organic or hybrid compounds, is their elastic scattering with the nuclei of the atoms forming the active material (mainly with hydrogen). This process results in the transfer of a portion of the neutron kinetic energy to the active material, which is then detectable. Specifically, the energy lost by the neutron is transferred to the nucleus with which it interacts, in particular, the relationship between the kinetic energies of the incident neutron ($E_N$) and of the recoil nucleus ($E_R$) can be expressed as:

$$\frac{E_R}{E_N} = \frac{4A}{(1+A)^2}cos^2\theta \quad (1)$$

where $A$ is the mass number of the target nucleus and $\theta$ is the recoil angle. Equation (1) indicates that the low-Z elements (e.g., hydrogen) are the ones which maximize the energy transfer between incident neutrons and recoil protons or nuclei.[1]

This mechanism can be exploited for the realization of two distinct classes of devices: i) indirect detectors, where a scintillating material rich in hydrogen (e.g., plastic scintillators) is coupled to a photodetector;[2–4] ii) direct detectors based on a semiconducting material optimized for neutron energy absorption. Direct detectors convert the radiation into an electrical output signal in a single step. This occurs when fast neutrons interact with low-Z elements contained in the semiconductor, generating recoil protons (or more generally, recoil nuclei) that release their energy by ionizing the material. The absorption of energy by the semiconductor induces the creation of electron/hole pairs, collected as an electrical output signal. The main advantages of the direct detection system, in comparison with the indirect one, are its superior efficiency and spatial resolution, resulting from the compact design of the device and lower cross talk. However, one of the most challenging limitations of fast neutron direct detectors

I. Fratelli, L. Basiricò, G. Napolitano, S. Cepić, A. Ciavatti, B. Fraboni
Department of Physics and Astronomy
University of Bologna
Viale Berti Pichat 6/2, Bologna 40127, Italy
E-mail: laura.basirico2@unibo.it
I. Fratelli, L. Basiricò, A. Ciavatti, B. Fraboni
INFN
Sezione di Bologna, Viale Berti Pichat 6/2, Bologna 40127, Italy
F. Pino, J. C. Delgado, S. Moretto, G. Maggioni, S. M. Carturan
Department of Physics and Astronomy
University of Padova
Via Marzolo 8, Padova 35121, Italy
E-mail: carturan@lnl.infn.it
S. Moretto
INFN
Sezione di Padova, Via Marzolo 8, Padova 35121, Italy
G. Maggioni, M. Cinausero, S. M. Carturan
INFN – Laboratori Nazionali di Legnaro
Viale dell'Università 2, Legnaro 35020, Italy

The ORCID identification number(s) for the author(s) of this article can be found under https://doi.org/10.1002/adfm.202502530

© 2025 The Author(s). Advanced Functional Materials published by Wiley-VCH GmbH. This is an open access article under the terms of the Creative Commons Attribution License, which permits use, distribution and reproduction in any medium, provided the original work is properly cited.

**DOI: 10.1002/adfm.202502530**

is that standard inorganic semiconductors currently employed as direct ionizing radiation detectors active layers (e.g., Si) are formed by high-Z elements, which according to Equation (1) absorb a small energy fraction from fast neutrons, leading to poor detection efficiency.

Therefore, the search for novel functional materials is an essential task for the development of an efficient class of fast neutron direct detectors. Organic semiconductors, which are primarily composed of low-Z elements, are considered as one of the most promising classes of semiconductors to target this goal. To date, some examples of solution-grown organic single crystals have been reported in literature for neutron detection. Kargar et al.[5] and Carman et al.[6] were the first demonstrating their ability to detect fast neutrons using perylene and rubrene single crystals respectively. More recently, Zhao et al. reported the performances achieved by two different organic single crystals (methyl 4-hydroxyben-zoate ($C_6H_5O$—$COOCH_3$, 4MHB) and 4-hydroxycyanobenzene ($C_6H_5O$-CN, 4HCB)).[7] The devices have been characterized under an $^{241}$Am-Be neutron source (energy range of 0.1–10.8 MeV, neutron activity of $6.6 \times 10^5$ n $s^{-1}$). The authors demonstrated how to tune the neutron detection efficiency by appropriate molecular tailoring. One important fact to take into account is that organic semiconductors typically exhibit poor transport properties (i.e low mobility-lifetime $\mu\tau$ product) which affect the efficient collection of the radiation induced charges and consequently the detection efficiency. Therefore, novel materials combining low-Z composition with a high $\mu\tau$ are still an open challenge.

In the last decade, metal halide perovskites emerged for their employment as ionizing radiation detectors' active layers thanks to their low trap density and high charge transport properties ($\mu\tau = [10^{-4}–10^{-2}]$ $cm^2$ $V^{-1}$).[8–12] They demonstrated excellent performances under different kinds of radiation such as X- and $\gamma$-rays, protons and charged particles.[13–20] Among metal halide perovskites, the hybrid organic-inorganic ones (structural formula $A^+B^+{}_2X^-{}_3$) are the most promising for fast neutron detection since they contain an organic cation (i.e., formed by low-Z elements) which acts as a fast neutron converter, producing detectable recoil protons/ions. The heavy atom-rich inorganic part of the material can then efficiently absorb the energy of the charged recoil protons/ions (by means of the ionization of the material) and directly provides an electrical output signal. Further, in 2D layered perovskites (general structural formula $(R\text{-}NH_3)_2A_{n-1}B_nX_{3n+1}$ with n = 1,2,3..., where R is an alkyl or aryl group), the organic cation is formed by long-chain amine with high hydrogen content, providing higher energy transfer from fast neutrons than 3D perovskites (e.g., methylammonium lead bromide $MAPbBr_3$, formamidinium lead bromide $FAPbBr_3$). 2D perovskites offer other important advantages such as higher environmental stability, reduced ion migration, and a lower dark current thanks to the quantum well-like energetic structure.[21–23] Despite such promising properties offered by this novel class of materials, they have been investigated mainly as scintillating materials.[24–27] To the best of our knowledge, only two very recent works report about the use of 2D perovskites, in form of single crystals, as direct fast neutron detectors. In 2023 Gao et al. demonstrated for the first time the fast neutron detection performance by employing a 2D perovskite single crystal of (butane- 1,4-diammonium) Lead Bromide ($BDAPbBr_4$).[28] The authors tested the device under an Am-Be neutron source achieving a good detecting response thanks to the high $\mu\tau = 3.3 \times 10^{-4}$ $cm^2$ $V^{-1}$ (higher than the one typically reported for organic single crystals) and high absorption fraction. The authors reported a sensitivity of $1.7 \times 10^{-4}$ nA $kW^{-1}$ (i.e., neutron induced current divided per the neutron reactor power source) and a signal saturation response time of 100 s. More recently, Panaccione et al. reported on the fast neutron direct detection by Methylhydrazinum Lead Trichloride $MHyPbCl_3$ single crystal.[29] They tested 330 µm thick single crystal under the neutron beam provided by a research nuclear reactor, providing also a further investigation on the discrimination ability of the detector by applying a combination of $\gamma$-rays and thermal neutrons shielding.

Here, we report direct fast neutron detection by a 2D perovskite thin film-based flexible device, made possible by the high density of low-Z elements (i.e., hydrogen and carbon atoms) forming the $PEA_2PbBr_4$ (PEA = $C_6H_5C_2H_4NH_3^+$) active layer. We measured an electrical output signal proportional to the neutron beam flux, allowing to monitor in real-time the intensity of the neutron field. Thanks to the thin film configuration (i.e., perovskite active layer [1–4] µm thick) we were able to minimize the cross section of interaction with high energetic $\gamma$-rays improving the discrimination capability with respect to the perovskite single crystal-based technology. Finally, the thin film configuration allows to envisage for a flexible and easily scalable detector, very appealing for personal dosimetry, where a compact, large area and wearable device is highly desirable and still not addressed at the state of the art.

Beyond their promising material properties and detection capabilities, the employment of $PEA_2PbBr_4$ and the possibility of realizing flexible fast neutron detectors open new avenues for applications where conventional rigid detectors are impractical due to weight, fragility, or geometrical constraints. Their lightweight and conformability make these novel detectors particularly appealing for personal dosimetry, enabling real-time dose monitoring for workers exposed to radiation in environments such as nuclear power plants, medical radiotherapy centers, and aerospace missions. In these scenarios, neutron fluxes typically range from $10^2$ to $10^4$ $n \cdot cm^{-2} \cdot s^{-1}$, and accurate long-term monitoring is crucial to ensure compliance with safety limits (e.g., 20 mSv per year for radiation workers).[30]

As an example, in space applications, fast neutrons generated by cosmic ray interactions with spacecraft materials represent a significant component of the radiation field. Here, flexible detectors integrated into garments, interior surfaces, or spacesuits could provide real-time monitoring improving the safety of the astronauts.[31,32] Moreover, in the medical field, particularly in proton therapy, secondary neutrons are produced as fragmentation products during radiation delivery and may pose secondary cancer risks; flexible detectors could be used for mapping these neutron fields directly on patients or equipment.[33,34]

In summary, the versatility, lightweight nature, and conformability of flexible fast neutron detectors enable their use in a wide range of practical scenarios where traditional detectors are not suitable.


© 2025 The Author(s). Advanced Functional Materials published by Wiley-VCH GmbH

16163028, 0, Downloaded from https://advanced.onlinelibrary.wiley.com/doi/10.1002/adfm.202502530 by Cambridge University Library, Wiley Online Library on [04/07/2025]. See the Terms and Conditions (https://onlinelibrary.wiley.com/terms-and-conditions) on Wiley Online Library for rules of use; OA articles are governed by the applicable Creative Commons License

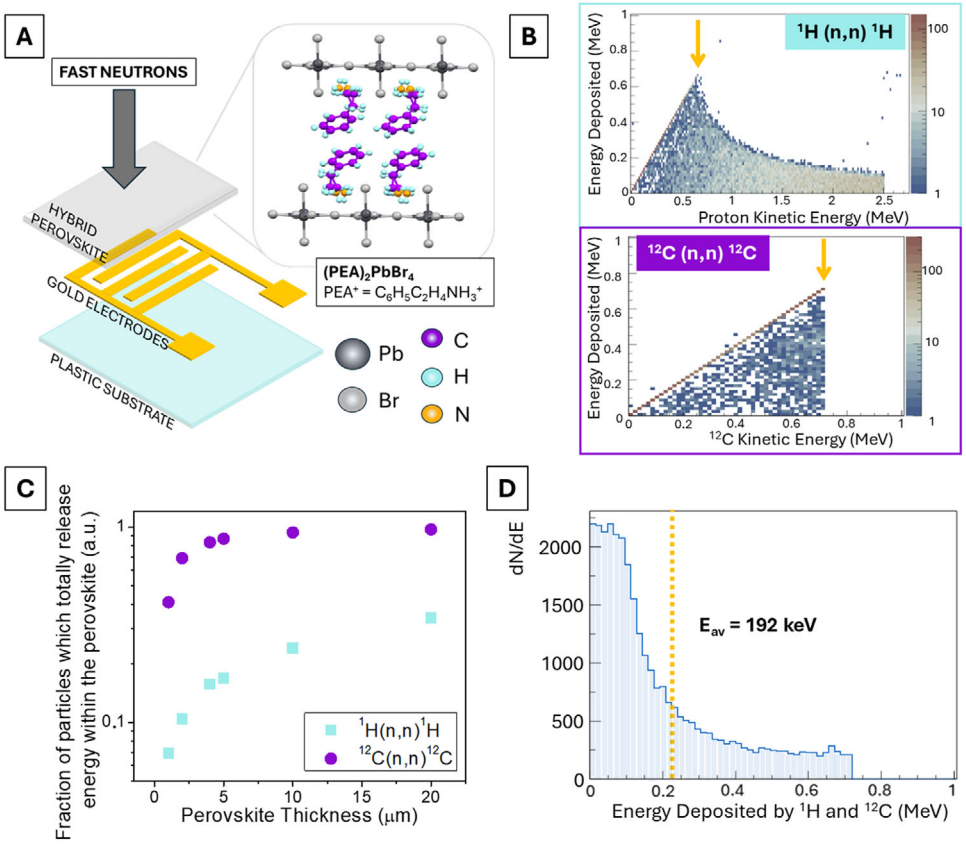


**Figure 1.** Fast Neutrons – Hybrid 2D perovskite interaction – Monte Carlo simulation. A) Schematic of the two terminal co-planar detector formed by gold interdigitated electrodes (L = 30 μm, W = 50 mm, pixel area = 2 × 2 $mm^2$) deposited onto flexible substrate (Kapton 50 μm thick) and $(PEA)_2PbBr_4$ thin film deposited by spin coating on the top. The inset shows the molecular structure of the $(PEA)_2PbBr_4$ 2D hybrid perovskite. B) Fast neutrons mainly interact with perovskite thin film by means of elastic scattering $^1H(n,n)^1H$ and $^{12}C(n,n)^{12}C$. The fraction of energy transferred through these interactions to recoil protons (up) and recoil carbon nuclei (bottom), and its deposition inside the 5 μm perovskite film, has been modelled by Monte Carlo simulation (Geant4). The energy absorbed by the semiconductor can be directly detected by the device as an electrical output signal. The yellow arrows indicate the highest energetic byproducts (i.e., recoil protons or carbon ions) able to release their entire energy within the 5 μm thick perovskite layer. C) Plot of the fraction of byproducts, i.e., recoil carbon nuclei (violet circles) and protons (cyano squares) able to release their whole energy within the semiconductor layer in function of if its thickness. D) Spectrum of the energy released inside a 5 μm thick perovskite layer after the irradiation with 2.5 MeV fast neutrons. The spectrum has been generated by Monte Carlo simulation (Geant4). For each event, the mean energy released inside the perovskite is 192 keV.

## 2. Results

The reported detectors have a co-planar architecture, with two ohmic contacts between the active layer and the electrodes. As it is shown in **Figure** 1A, two interdigitated gold electrodes (L = 30 μm, W = 50 mm, pixel area = 2 × 2 $mm^2$) have been deposited by thermal evaporation onto a 50 μm polyimide substrate to guarantee the mechanical flexibility of the final device.[13,35] The 2D perovskite (i.e., $PEA_2PbBr_4$) thin films have been deposited by spin coating on the top of the electrodes forming a microcrystalline film. Details on the fabrication procedures are reported in the Experimental Section. The molecular structure of the 2D perovskite is reported in Figure 1A, showing the high density of hydrogen and carbon atoms present in the long amine chain forming the organic interlayer of the molecule (i.e., the hydrogen and carbon densities are respectively 4.25 × $10^{22}$ $cm^{-3}$ and 2.84 × $10^{22}$ $cm^{-3}$). The large presence of such low-Z elements is comparable with other active materials (e.g., plastic and liquid scintillators, organic semiconductors and other organic metal halide perovskites, see Table S1 (Supporting Information) section[29]) that have been reported as active layers for fast neutron detectors. To model quantitatively the interaction mechanism, Monte Carlo simulations (using the toolkit Geant 4)[36–38] have been performed (more details in Experimental Section). The neutron energy has been set to 2.5 MeV since it is comparable to the mean energy of the fission reactor,[39] and also, it corresponds to the neutron energy emitted by a Deuterium-Deuterium (D-D) neutron generator, which is commonly employed in fast neutron applications. Figure 1B reports plots of the computed energy deposited within a 5 μm thick perovskite layer by recoil protons/fragments due to the elastic scattering of the fast neutrons with the hydrogen (top) and carbon (bottom) atoms. It is evident how a portion of the recoil protons/fragments with a high kinetic energy may not be able to release their entire energy within the film, as they escape from it (83% of protons and 13% of carbon ions considering the 5 μm thick perovskite layer). Figure 1C


© 2025 The Author(s). Advanced Functional Materials published by Wiley-VCH GmbH

16163028, 0, Downloaded from https://advanced.onlinelibrary.wiley.com/doi/10.1002/adfm.202502530 by Cambridge University Library, Wiley Online Library on [04/07/2025]. See the Terms and Conditions (https://onlinelibrary.wiley.com/terms-and-conditions) on Wiley Online Library for rules of use; OA articles are governed by the applicable Creative Commons License

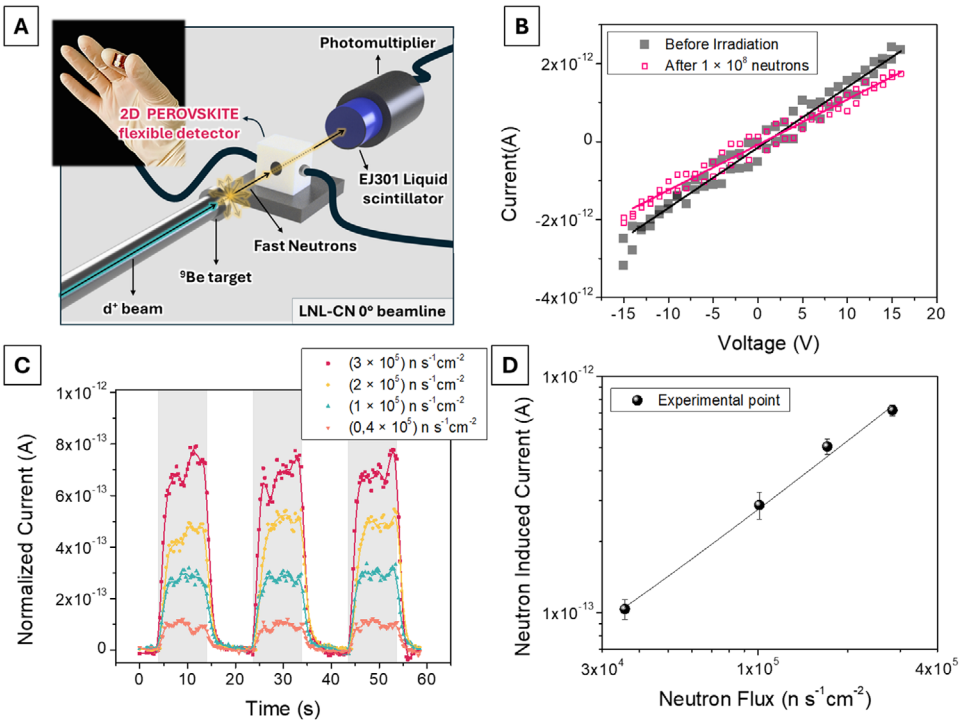


**Figure 2.** Fast neutron irradiation. A) Sketch of the 0° beamline at Laboratories of Legnaro (INFN-LNL) in the CN Van de Graaff accelerator. The fast neutrons were produced by a 5 MeV deuterium accelerated beam (current range [1–30] nA) impinging onto a $^{9}$Be target ($^{9}$Be(d,n)$^{10}$B). Our detector was enclosed in a dark box and placed in front of the beamline output window at 10 cm from the target. The neutron field flux was monitored by a 2″ × 2″ EJ-301 liquid scintillator cell coupled to a PMT placed at 2 m from the Be target. In the inset, the picture shows a flexible 2D hybrid perovskite-based detector. B) Current–Voltage characteristics of a (1.90 ± 0.04) µm thick perovskite-based device before (black solid square) and after $10^8$ total neutrons irradiating the device (pink void square). The irradiation causes a decrease of ≈25% of electrical conductivity. C) Dynamic response of the detector irradiated by three subsequent 10 s irradiation cycles (grey shadows) for four different neutron field flux ([0.4; 1; 2; 3] · $10^5$ n s$^{-1}$ cm$^{-2}$). The sample was biased at 15 V (0.5 V µm$^{-1}$). D) The neutron induced current scales with the neutron field intensities. The maximum slope of the first derivative of the curve represents the sensitivity of the detector S = (2.6 ± 0.2) · $10^{-18}$ C n$^{-1}$.

shows the increase of fraction of byproducts able to release their whole energy within the semiconductor layer with the increase of its thickness. In other words, by increasing the perovskite thickness it is possible to increase the percentage of recoil protons and carbons which can release their entire amount of energy within the film. Since the energy in this interaction is transferred via ionization, the process is more efficient for higher-Z and more massive byproducts (i.e., carbon with respect to hydrogen). Moreover, as it is illustrated in Figure S1 (Supporting Information), each interaction event (via elastic scattering on hydrogen and carbon nuclei) results in significant ionization through high-LET byproducts. For instance, from these simulations we calculated that the mean energy value released by each event 5 µm-thick perovskite is on the order of 192 keV (Figure 1D).

In this work, we tested different devices based on three increasing perovskite's thicknesses. The devices have been realized onto flexible polyimide substrates to guarantee the flexibility of the detector as it is shown in the picture reported in **Figure 2A** and in the characterization under mechanical stress reported in Figure S2 (Supporting Information). After a careful optimization of the deposition procedure well described in Experimental Section, we obtained uniform and homogeneous films (film profile extraction and top-view / cross-section SEM images are reported in Figure S3, Supporting Information) by decreasing the spin coating velocity (namely 6000 rpm, 2000 rpm and 1000 rpm), corresponding to thickness of the final layer of (0.92 ± 0.01) µm, (1.90 ± 0.04) µm and (4.05 ± 0.06) µm respectively. In Figure S3 (Supporting Information) we report the current-voltage characteristics measured for the three devices. These all show an ohmic and uniform behavior for the entire set of samples. The electrical conductivity values have been calculated as ($\sigma = \frac{1}{R_s t}$ ) and they are (3.1 ± 0.1) · $10^{-11}$ S m$^{-1}$, (1.4 ± 0.1) · $10^{-11}$ S m$^{-1}$ and (0.29 ± 0.01) · $10^{-11}$ S m$^{-1}$ respectively from the thinnest to the thicker film. By increasing the thickness of the perovskite, the conductivity of the polycrystalline film degrades probably due to the poorer uniformity and homogeneity of the ticker polycrystalline film shown in the SEM images (Figure S3, Supporting Information). The mobility lifetime product for analogous devices (same geometry and 2 µm thick $PEA_2PbBr_4$) is in the order of $10^{-5}$ cm$^2$V$^{-1}$, as we reported in our previous work,[35] which is comparable to the typical value of one of the benchmark materials employed for large-area radiation detection applications, such as amorphous selenium (α-Se).[40]

To experimentally assess the neutron detecting performance of the devices, we tested them under the fast neutron field provided by the Van der Graaff accelerator at the National


© 2025 The Author(s). Advanced Functional Materials published by Wiley-VCH GmbH

16163028, 0, Downloaded from https://advanced.onlinelibrary.wiley.com/doi/10.1002/adfm.202502530 by Cambridge University Library, Wiley Online Library on [04/07/2025]. See the Terms and Conditions (https://onlinelibrary.wiley.com/terms-and-conditions) on Wiley Online Library for rules of use; OA articles are governed by the applicable Creative Commons License

Institute of Nuclear Physics – Legnaro Laboratory (INFN-LNL, CN accelerator, 0° beamline). Here, a 5 MeV Deuterium beam has been employed (Deuterium current = [1–30] nA) and has been directed onto a $^{9}$Be target. The used target, designed for the MUNES (MUltidisciplinar NEutron Source) project[41] is a three-layer structure composed of a beryllium film with a thickness of 50 µm, a 2-mm-thick vanadium layer needed to suppress blistering phenomena and a copper bulk for heat-sink purposes. The fast neutrons are produced by the $^{9}$Be(d,n)$^{10}$B reaction (energy spectrum in the range [1–4] MeV and neutron flux = [0.4–3] · $10^{5}$ n $s^{-1}$ $cm^{-2}$ as already reported in literature by Meadovws et al.)[42] at the end of the beamline, and the perovskite detector has been placed 10 cm far from the emission point. The detector has been electrically connected and enclosed in an experimental box to keep the device in dark during the irradiation. The flux and the energy spectrum of the neutron field have been monitored during the experiment by an EJ-301 liquid scintillator (from Eljen technologies Texas-US) coupled to a Hamamatsu photomultiplier R7724-100 (operated at −1200 V) placed behind the perovskite detector at 2 m from the Be target position. Figure 2A details the experimental setup and reports a picture of the flexible perovskite thin film-based neutron detector.

As an example, Figure 2B reports the current-voltage characteristics of one of the devices (perovskite thickness = (1.90 ± 0.04) µm) before and after the irradiation test. The high resistivity of the 2D perovskite detector ($\rho$ = (1.1 ± 0.5) • $10^{12}$ Ω cm) guarantees a low dark current, i.e., a crucial property of a well-performing radiation detector. After irradiation with $10^{8}$ fast neutrons, the electrical conductivity shows a degradation of 25%, however preserving an ohmic behavior. The long-term operational stability of $PEA_2PbBr_4$ thin films under ionizing radiation and environmental exposure is also reported in Figure S5 (Supporting Information). This devices demonstrated negligible degradation on the detection capabilities after 6 months of storage in ambient conditions (i.e., air and room temperature) and also after multiple X-ray irradiation cycles up to 9.6 Gy of total dose. In fact, 2D perovskite materials typically exhibit superior environmental stability compared to their 3D counterparts thanks to their layered structure which increases the hydrophobicity of the material and provides an effective barrier against moisture ingress.[43] Besides, hybrid perovskite materials recently exhibit good radiation tolerance thanks to their good self-healing properties after radiation damage. In particular, A. R. Kirmani at al. recently demonstrated that ionization energy loss mechanisms, as the ones occurring after the primary interaction between fast neutrons and hybrid perovskite, can actually promote defect healing processes in this class of materials.[44]

Figure 2C shows the dynamic response of the same detector under fast neutron irradiation biased in direct current mode at 15 V (0.5 V $µm^{-1}$). The electrical current has been monitored in real-time (see detail in Experimental Section). The detector has been irradiated by three subsequent 10 s irradiation cycles (grey shadows) increasing the fast neutron flux ([0.4; 1; 2; 3] • $10^{5}$ n $s^{-1}$ $cm^{-2}$). During irradiation the current flowing in the detector channel steeply increases due to the release of energy within the semiconductor and the consequent generation of excess charges. The radiation induced current increases with the flux of neutrons following a sublinear trend as shown in the plot in Figure 2D. In general, in photoconductors where the detection process is strongly governed by a trap-mediated internal amplification mechanism known as photoconductive gain, the radiation induced current commonly exhibit this sublinear trend as a function of the radiation flux. In these devices, the PG intrinsically amplifies the detecting response of the devices by a gain factor $G$ which is defined as the ratio between the recombination time $\tau_r$ of the minority carrier trapped and the transit time $\tau_t$ of the majority carrier across the channel of the device ($G = \tau_r / \tau_t$). In these devices the $G$ factor typically decreases with increasing radiation flux (whether referring to ionizing radiation dose rate or visible light power). This behavior is primarily attributed to the progressive filling of trap states that mediate the PG effect. In fact, as the radiation flux increases, deep trap states for minority carriers gradually become filled and the minority carriers start to be trapped by shallower defects. This leads to a reduction in effectiveness of the photoconductive gain activation (i.e., the recombination time $\tau r$ of the minority carrier trapped in shallower traps is lower) and, consequently, to a decrease in the detecting signal.[45–47] We calculated the sensitivity of the detector as the maximum slope of the first derivative of the curve S = (2.6 ± 0.2) • $10^{-18}$ C $n^{-1}$.

This device provides a stable response also when irradiated by longer exposures (60 s, 2.4 · $10^{5}$ n $s^{-1}cm^{-2}$, 1.44 · $10^{7}$ neutrons in total; **Figure 3A**). The rise and falling times, calculated as the time for reaching the 90% of the signal starting from the 10% (the opposite for the falling time) result respectively $\tau_{rise}$ = (1.6 ± 0.3) s and $\tau_{fall}$ = (4.2 ± 0.3) s. These values are comparable with the rise and falling times measured by exposing the device under 5 MeV proton irradiation that we recently reported,[48] suggesting that such time-scales intrinsically characterize the heavy particle detection dynamics of this 2D perovskite when it absorbs energy due to ionization processes. In fact, as discussed above, the photoconductive gain arising in these photoconductors relies on the presence of long-lived trap states for minority carriers which induces an intrinsic amplification of the detecting signal ($PG$). The characteristic rise and fall times of the detector signal are therefore strongly influenced by the trapping and detrapping timescales of these trap states (i.e., the reach of a dynamic equilibrium between the filling and recombination of these states). Further optimization of the response times would thus require a deep investigation into the nature, distribution, and energy depth of the trap states, followed by a device engineering to tailor their properties. Noteworthy, the here presented devices show much faster responses than other devices based on hybrid perovskites previously reported in literature by Gao et al. for similar irradiation (i.e., 100 s to reach the saturation of the response under fast neutron irradiation).[28] Further, the detector shows a reproducible and repeatable response when exposed to four subsequent identical irradiation cycles, decreasing and then increasing the neutron field flux in the range [1.8–5.7] · $10^{5}$ n $s^{-1}$ $cm^{-2}$ (Figure 3B).

To assess the charge collection properties of the here proposed thin-film detectors, we investigated their response upon different applied biases. In Figure 3C we report the sensitivity of three devices with different perovskite layer thicknesses, and at three different collection electric fields 0.1, 0.25, 0.5 V $µm^{-1}$ (i.e., 3, 7.5, 15 V bias) respectively. The sensitivity is higher for the thicker films, because of the larger perovskite interaction volume. Interestingly, the response does not show instead a clear trend with the


© 2025 The Author(s). Advanced Functional Materials published by Wiley-VCH GmbH

16163028, 0, Downloaded from https://advanced.onlinelibrary.wiley.com/doi/10.1002/adfm.202502530 by Cambridge University Library, Wiley Online Library on [04/07/2025]. See the Terms and Conditions (https://onlinelibrary.wiley.com/terms-and-conditions) on Wiley Online Library for rules of use; OA articles are governed by the applicable Creative Commons License

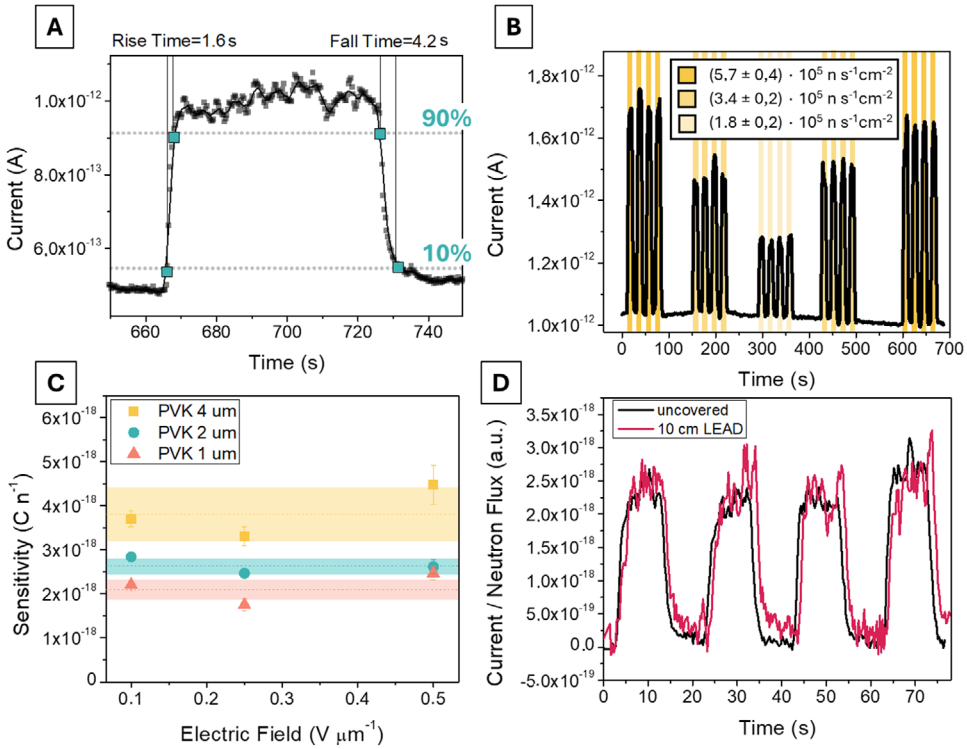


**Figure 3.** Characterization of the fast neutron detector. A) 60 s long exposure at $2.4 \cdot 10^5$ n s$^{-1}$. The device is (1.90 ± 0.04) μm thick and biased at 0.1 V μm$^{-1}$. The rise time ($\tau_{rise}$ = 1.6 s) and the fall time ($\tau_{fall}$ = 4.2 s) are considered as the temporal interval in which the detector switch from the 10% and the 90% of the detecting signal. B) Response of the device irradiated by 4 subsequent 10 s irradiation cycles at the flux: $5.3 \cdot 10^5$ n s$^{-1}$; $3.2 \cdot 10^5$ n s$^{-1}$; $1.7 \cdot 10^5$ n s$^{-1}$ cm$^{-2}$ and back. C) Sensitivity obtained by applying different electric field to the device. Three different samples have been tested with three different thicknesses (yellow squares: (4.05 ± 0.06) μm; cyano circles: (1.90 ± 0.04) μm; pink triangles: (0.92 ± 0.01) μm). D) Dynamic response to fast neutrons while the detector was placed in front of the beamline directly (black line) and by interposing 10 cm thick lead slab between the radiation beam output window and the detector. The current response is normalized by the effective number of fast neutrons, to consider the attenuation of 50% of the neutron field intensity by the lead shielding.

applied bias, suggesting that response saturation is reached even at low voltages (i.e., 3 V) for the three different perovskite thicknesses. Such a feature is desirable to target wearable personal dosimeters, where low-voltage operation is a mandatory requirement.

Another important requirement for neutron detectors is low $\gamma$-ray sensitivity. Since the generation of neutrons often occurs with emission of $\gamma$-rays, it is important to not count the false neutron events from $\gamma$-ray absorption. This can be done following different strategies, for example by using a material formed mainly by light elements that have low $\gamma$-ray absorption coefficient (e.g., organic materials) or by using pulse shape discrimination enabled by the different time scales between a neutron signal pulse and a $\gamma$ signal pulse.[49]

Here, to assess the $\gamma$-rays discrimination capability, we exposed the detector to four subsequent fast neutron irradiation cycles (neutron flux = $8.0 \cdot 10^4$ n s$^{-1}$ cm$^{-2}$; bias = 15 V) with and without interposing 10 cm thick lead slab between the detector and the neutron (and also gamma-ray) emission point. This shielding tool strongly reduces the $\gamma$-ray intensity to 1% of the initial value. This attenuation factor has been calculated by simulating the interaction between a 1 MeV monoenergetic $\gamma$-ray beam (i.e., good estimation of the average energy value of the gamma spectrum produced by the $^9$Be(d,n)$^{10}$B reaction, coming from the measurement done with the EJ-301 scintillation detector) with 10 cm of lead shielding. Figure 3D shows how the detector response normalized for the flux of fast neutron fields remains unchanged with and without the lead shielding, clearly indicating that the electrical current increase under irradiation is totally due to the fast neutron interaction with the perovskite. In fact, even if fast neutrons and 1 MeV gamma rays have similar interaction probabilities in a $PEA_2PbBr_6$ perovskite thin film (i.e., in 1 μm of perovskite the attenuation fractions are 0.0017% for neutrons and 0.0014% for 1 MeV gamma),[50] the selectivity shown by these devices is based not only on the attenuation coefficient, but on the different linear energy transfer of the secondary particles generated by the primary interactions of fast neutrons or gamma rays within the perovskite (i.e., respectively recoil protons/ions or Compton electrons) as shown by the sketch reported in Figure S1 (Supporting Information). For instance, while for each event of interaction with fast neutrons the recoil protons and ions can release 192 keV in 5 μm of perovskite (as reported in Figure 1D), for each Compton scattering of 1 MeV gamma ray, the total energy released by secondary electrons is ≈1.5-2 keV.[51] Thus, although the interaction probabilities with 1 MeV photons and fast neutrons are similar, for each event the energy transfer from the byproducts to the perovskite thin film differs by 2 orders of magnitude, providing the basis for selectivity between gamma rays


© 2025 The Author(s). Advanced Functional Materials published by Wiley-VCH GmbH

16163028, 0, Downloaded from https://advanced.onlinelibrary.wiley.com/doi/10.1002/adfm.202502530 by Cambridge University Library, Wiley Online Library on [04/07/2025]. See the Terms and Conditions (https://onlinelibrary.wiley.com/terms-and-conditions) on Wiley Online Library for rules of use; OA articles are governed by the applicable Creative Commons License

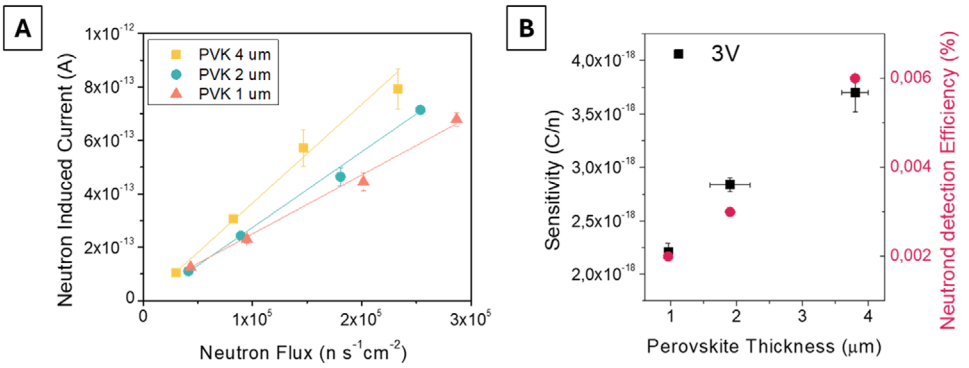


**Figure 4.** Impact of the perovskite thickness on the detecting performance. A) Neutron induced current by different neutron fluxes for three different samples deposited at different speeds (yellow squares: (4.05 ± 0.06) μm, 1000 rpm; blue light circles: (1.90 ± 0.04) μm, 2000 rpm; pink triangles: (0.92 ± 0.01) μm, 6000 rpm). The applied electric field is 0.1 V $\mu m^{-1}$. B) The sensitivity (black squares) and simulated neutron detection efficiency (pink circles) of the three samples as a function of their thicknesses (i.e., the detector active volume).

and fast neutrons detection in our device. Finally, to further experimentally confirm the selectivity of our detector, we tested the devices under gamma rays produced by a $^{60}Co$ radioactive source (Activity = 1000 kBq) (see Figure S6, Supporting Information). At the energy and fluxes comparable to what was present in the mixed field at the fast neutron facility, a negligible induced current can be appreciated during the exposure to the gamma rays, confirming the selectivity of the response offered by this class of detectors.

**Figure 4** shows the impact of the active layer thickness on the detection performances. In Figure 4A reports the neutron induced current as a function of the neutron field fluxes for three samples of different perovskite thicknesses biased at 3 V. The measured sensitivities for the samples are $S_{4\,\mu m}$ = (3.7 ± 0.2) • $10^{-18}$ C $n^{-1}$, $S_{2\,\mu m}$ = (2.8 ± 0.1) • $10^{-18}$ C $n^{-1}$, $S_{1\,\mu m}$ = (2.2 ± 0.1) • $10^{-18}$ C $n^{-1}$. This result can be better understood in the light of Figure 4B, showing how by increasing the active layer thickness we boost the cross section of interaction with fast neutrons and, consequently, the neutron detection efficiency scales accordingly. The neutron detection efficiency is commonly used in the literature as the most reliable and standardized parameter to benchmark the performance of fast neutron detectors and it has been estimated from the simulations discussed in Figure 1 and it has been calculated as the ratio between the number of interaction events within the active layer and the total number of neutrons passing through the device (which were calculated from the Monte Carlo simulation performed with Geant4 and reported in Figure 1). As it is reported in the Table T2 (Supporting Information) The efficiency of our detectors is comparable with the typical values reported in literature for direct and indirect detectors based on hybrid and organic materials and one order on magnitude lower than the value reported for CVD diamond.[7,24,29,52] Plots of sensitivity as a function of the perovskite thickness for different biasing conditions are reported in Figure S7 (Supporting Information), confirming the same trend for all the three applied electric fields.

Figure 4 clearly shows that the detector is able to collect from the entire active layer thickness, even at low bias and even for the thicker film, despite the electrodes' planar configuration, thanks to the extension of electric field fringes far from the electrodes-perovskite interface. This is further supported by the finite-element simulations reported in Figure S8 (Supporting Information) where it is clearly shown that the electric field distribution benefits from strong fringing fields, allowing efficient carrier collection throughout the full thickness of the perovskite layer, even in our thickest configurations.

This result indicates that the optimization of the deposition procedure and the tuning of the active layer thickness is a promising route to boost the detecting efficiency of this material technology. On the other hand, two important limitations are worth to be considered: (i) this class of perovskites contains lead and heavy elements in the inorganic part, and increasing the thickness of the semiconductor layer also means increasing the attenuation fraction of $\gamma$-rays, which reduces the discrimination capability of the detector in the mixed field. One possibility to reduce the average Z of the perovskite (i.e., improving the selectivity also in thicker films) could be based on the employment of the lead-free 2D hybrid perovskites based on Sn ($Z_{Pb}$ = 82; $Z_{Sn}$ = 50).[53,54] This approach would also mitigate issues related to material toxicity and environmental impact, paving the way for the substitution of lead with less hazardous B-site metals; (ii) using thick films causes the lowering of charge transport properties and collection efficiency of the device (as shown in Figure S4, Supporting Information), affecting thus the collection of excess charges from the whole active volume. For instance, Gao et al.[28] collected pulse-height spectra of a perovskite single crystal-based detector ($BDAPbBr_4$) under alpha particles and $\gamma$-rays radioactive sources ($^{241}Am$ and $^{137}Cs$ respectively). Despite the higher crystallinity and higher charge transport properties of single crystals compared with our polycrystalline films, they observed a large difference between alpha particles and $\gamma$-rays detection. They justified this difference assuming that alpha particles interact with the materials at a much shallower depth than $\gamma$-rays and thus the charge collection from electrodes is much easier in the case of alpha particles detection.[28] Commonly, in polycrystalline films where the long-range order is poorer compared to the single crystals, the charge transport is dramatically reduced far from the electrodes, thus it is not convenient to increase too much the film thickness.

In conclusion, to maximize the detection efficiency of thin film perovskite detectors a trade-off between the maximization of the active volume, the effective charge collection, the discrimination


© 2025 The Author(s). Advanced Functional Materials published by Wiley-VCH GmbH

16163028, 0, Downloaded from https://advanced.onlinelibrary.wiley.com/doi/10.1002/adfm.202502530 by Cambridge University Library, Wiley Online Library on [04/07/2025]. See the Terms and Conditions (https://onlinelibrary.wiley.com/terms-and-conditions) on Wiley Online Library for rules of use; OA articles are governed by the applicable Creative Commons License

capability and the preservation of mechanical flexibility and scalability onto large areas must be targeted.

## 3. Conclusion

In this work, we report on the direct detection of fast neutrons by innovative detectors based on hybrid 2D perovskite thin films. This novel class of material recently demonstrated, in the single crystal form, a good potential for the detection of fast neutrons, thanks to the high density of low-Z elements forming the cation spacer, which maximize the fraction of energy transferred by the neutrons through elastic scattering, combined with proper semiconducting properties of charge transport. Here, $PEA_2PbBr_4$ perovskite active layer has been deposited from solution onto a flexible polymeric substrate forming a thin polycrystalline active layer. By tuning the fabrication conditions, we varied the semiconductor thickness and optimized the film quality, enhancing the final detection efficiency. By accurately and carefully increasing the active volume we boosted the performances of the detector, achieving a stable and reproducible response and reaching a maximum sensitivity of $S = (4.5 \pm 0.4) \bullet 10^{-18}$ C $n^{-1}$. The thin film configuration of our devices brings several innovative advantages: i) the device can be efficiently operated at low voltages targeting wearable and personal dosimetry; ii) the low thickness of the active layer limits the absorption of $\gamma$-rays and enhances the discrimination capability of this technology in mixed fields; iii) the perovskite active layer can be deposited from solution by low-temperature and easy-scalable deposition techniques envisaging the realization of flexible and large-area detecting systems.

## 4. Experimental Section

*Device Fabrication*: The metal electrodes were fabricated on 50 µm thick polyimide substrate by lithographic techniques. Before electrodes deposition the substrates were cleaned by subsequent ultrasonic baths in $H_2O$ and soap, deionized H2O and isopropyl alcohol. A positive photoresist (S1818) was then spin coated on the substrate at 4000 rpm for 60 s. The layout has been projected exposing the resist through an optical Microwriter (ML3Durham Magneto Optic). The resist has been developed by MICROPOSIT MF-139 developer and then rinsed with deionized water. Electrodes were formed by 5 nm of Chromium and 45 nm of Gold thus deposited through thermal vacuum evaporation and patterned by dipping the whole structure into acetone bath for 4 h.

For the perovskite preparation, $C_6H_5C_2H_4NH_3Br$ (PEABr, Sigma–Aldrich >98%) and $PbBr_2$ (Sigma–Aldrich >98%) were mixed inside a nitrogen filled glove box in N,N-dimethylformamide (DMF, Sigma–Aldrich 99.8% anhydrous) to prepare a 1 M solution with 2:1 molar ratio. The solution was mixed thoroughly for 5 h until complete dissolution of the precursors.

The perovskite has been deposited by spin coating (1000 rpm 10s; 2000 rpm 10s; 6000 rpm 10s; 10 min of annealing at 60 °C). During the spin coating an antisolvent (i.e., chlorobenzene) has been dropped on the substrate after the perovskite solution.

*Monte Carlo Simulation*: Monte Carlo simulations were performed using the toolkit Geant4.[36–38] A simple geometrical model of the sensor was built in the G4VUserDetectorConstruction class. It consisted on thin layer of 2 mm-side with a variable thickness (1, 2, 4, 5 10 and 20 µm) and a detailed composition and density of $PEA_2PbBr_4$ ($PEA = C_6H_5C_2H_4NH_3^+$, density = 2.27 g $cm^{-3}$). The neutron transport was managed with the high precision neutron model for low energy neutrons (<20 MeV) included on the QGSP_BERT_HP physics list. The neutrons were emitted as a parallel field of radiation covering the all surface of the sensing material. The initial energy of the neutrons was constant at 2.5 MeV. A maximum of $4 \times 10^8$ primary neutrons were simulated during each run. With the use of the G4Step and G4Track classes (implemented on the G4UserSteppingAction class), it was possible to track the history of each event (primary and secondary particles) during each step, and for example, to access to the type of interaction, secondary particles created, kinetic energy of the particles, deposited energy in the volume of interest, etc.

*Profilometer Characterization*: Film thickness was estimated by extracting a line profile across the edge between the perovskite layer and the Kapton substrate. Profiles were acquired using the GBS smartWLI white light interferometer with a 10x magnification lens. The subsequent data analysis was carried out with Mountains 9 software.

*Neutron Irradiation*: The detectors have been tested under the fast neutrons provided by the Van der Graaff accelerator at the National Institute of Nuclear Physics – Legnaro Laboratory (INFN-LNL, CN accelerator, 0° beamline). A 5 MeV Deuterium beam has been employed (Deuterium current = [1–30] nA) and has been directed onto a $^9$Be target. The Deuterium current has been monitored using a Faraday cup connected to an amperometer Keithley 414S. The fast neutrons field was produced via the $^9$Be(d,n)$^{10}$B reaction (energy in the range [1–4] MeV and neutron field fluxes = [[0.4-3] · $10^5$] n $s^{-1}$ $cm^{-2}$). The perovskite detector has been placed 10 cm far from the position of the Be target (emission point of the neutrons). The flux and the energy spectrum of the neutron field have been monitored during the experiment using a 2″ x 2″ liquid scintillator cell (EJ-301) coupled to a R7724-100 Hamamatsu PMT and placed behind the perovskite detector 2 m away from the Be target position.

The perovskite-based detector has been enclosed in a plastic box to prevent the illumination of the device during the irradiation and to electrically connect it to a commercial electrometer.

*SEM Images*: The images were acquired by using a Cambridge Stereoscan 360 SEM, operating at 20 kV. The cross-section samples were obtained by cutting the Kapton substrate at the edge and pulling apart two pieces by hand.

*Finite Element Simulation*: To analyze the electric field distribution across the $PEA_2PbBr_4$ perovskite channel in our planar detector architecture ANSYS Maxwell 2D package was employed. It simulated a transversal portion of the channel by selecting the cross section of the material between two fingers of the electrodes. The $PEA_2PbBr_4$ parameters used in the simulations were selected based on experimental and literature data: the conductivity value of the order of $1 \times 10^{-11}$ S $m^{-1}$ (in accordance was adopted with the values extracted from the *I–V* measurements reported in the manuscript in Figure S4, Supporting Information), and a relative permittivity $\varepsilon r = 3$, in line with values recently reported in the literature.[55–59]

## Supporting Information

Supporting Information is available from the Wiley Online Library or from the author.

## Acknowledgements

I.F, L.B., A.C., S.M.C., G.M., M.C., S.M., and B.F. acknowledge funding from INFN through the CSN5 BEYOND Grant for Young Researcher. I.F. received funding from the European Union's Horizon Europe research and innovation program under the Marie Skłodowska-Curie grant agreement No 101105245. L.B. and G.N. acknowledge the RELOAD project funded by Fondazione Cariplo and Fondazione CDP, grant no. 2022-1834. The authors would like to acknowledge Anna Selva, Luca Bellan and Luca Maran for the precious support provided for the measurements at CN accelerator in Laboratori Nazionali di Legnaro (INFN). The authors would like to acknowledge Luca Pasquini and Alberto Piccioni for SEM images at the Department of Physics and Astronomy, University of Bologna. The authors would like to acknowledge M. Chiari for the precious support provided for the aging measurements performed under 5-MeV proton irradiation at the LABEC (INFN-Florence).

Open access publishing facilitated by Universita degli Studi di Bologna, as part of the Wiley - CRUI-CARE agreement.


© 2025 The Author(s). Advanced Functional Materials published by Wiley-VCH GmbH

16163028, 0, Downloaded from https://advanced.onlinelibrary.wiley.com/doi/10.1002/adfm.202502530 by Cambridge University Library, Wiley Online Library on [04/07/2025]. See the Terms and Conditions (https://onlinelibrary.wiley.com/terms-and-conditions) on Wiley Online Library for rules of use; OA articles are governed by the applicable Creative Commons License

## Conflict of Interest

The authors declare no conflict of interest.

## Data Availability Statement

The data that support the findings of this study are available from the corresponding author upon reasonable request.

## Keywords

2D perovskites, detectors, fast neutrons, thin films

Received: January 25, 2025
Revised: May 4, 2025
Published online:

[1] W. Li, M. Li, Y. He, J. Song, K. Guo, W. Pan, H. Wei, W. Pan, *Adv. Mater.* **2024**, *36*, 2309588.
[2] R. Lopez, W. M. Steinberger, N. Giha, P. Marleau, S. D. Clarke, S. A. Pozzi, *Nucl. Instrum. Methods Phys. Res. A* **2022**, *1042*, 167407.
[3] F. Pino, M. Polo, J. C. Delgado, G. Mantovani, S. M. Carturan, D. Fabris, D. Brunelli, L. Pancheri, A. Quaranta, S. Moretto, *Radiat. Phys. Chem.* **2023**, *202*, 110494.
[4] N. Zaitseva, B. L. Rupert, I. Pawełczak, A. Glenn, H. P. Martinez, L. Carman, M. Faust, N. Cherepy, S. Payne, *Nucl. Instrum. Methods Phys. Res. A* **2012**, *668*, 88.
[5] A. Kargar, E. V. Van Loef, L. Cirignano, K. S. Shah, S. Member, *2011 IEEE Nuclear Science Symp. Conf. Record*, Valencia, Spain, October **2011**.
[6] L. Carman, H. P. Martinez, L. Voss, S. Hunter, P. Beck, N. Zaitseva, S. A. Payne, P. Irkhin, H. H. Choi, V. Podzorov, *IEEE Trans. Nucl. Sci.* **2017**, *64*, 781.
[7] D. Zhao, P. Cai, W. Cheng, W. Jia, B. Zhang, M. Zhu, L. Liu, X. Ouyang, P. Sellin, W. Jie, Y. Xu, *Adv. Funct. Mater.* **2022**, *32*, 2108857.
[8] J. Zhao, L. Zhao, Y. Deng, X. Xiao, Z. Ni, S. Xu, J. Huang, *Nat. Photonics* **2020**, *14*, 612.
[9] Y. He, I. Hadar, M. G. Kanatzidis, *Nat. Photonics* **2022**, *16*, 14.
[10] A. Jana, S. Cho, S. A. Patil, A. Meena, Y. Jo, V. G. Sree, Y. Park, H. Kim, H. Im, R. A. Taylor, *Mater. Today* **2022**, *55*, 110.
[11] H. Wei, J. Huang, *Nat. Commun.* **2019**, *10*, 1066.
[12] L. Basiricò, A. Ciavatti, B. Fraboni, *Adv. Mater. Technol.* **2021**, *6*, 2000475.
[13] L. Basiricò, I. Fratelli, M. Verdi, A. Ciavatti, L. Barba, O. Cesarini, G. Bais, M. Polentarutti, M. Chiari, B. Fraboni, *Adv. Sci.* **2023**, *10*, 2204815.
[14] L. Zhao, Z. Shi, Y. Zhou, X. Wang, Y. Xian, Y. Dong, O. Reid, Z. Ni, M. C. Beard, Y. Yan, J. Huang, *Nat. Photonics* **2024**, *18*, 250.
[15] Y. He, I. Hadar, M. G. Kanatzidis, *Nat. Res.* **2022**, *16*, 14.
[16] K. R. Dudipala, T. H. Le, W. Nie, R. L. Z. Hoye, *Adv. Mater.* **2024**, *36*, 2304523.
[17] Y. Wu, J. Feng, Z. Yang, Y. Liu, S. Liu, *Adv. Sci.* **2023**, *10*, 2205536.
[18] F. Liu, R. Wu, J. Wei, W. Nie, A. D. Mohite, S. Brovelli, L. Manna, H. Li, *ACS Energy Lett.* **2022**, *7*, 1066.
[19] F. Liu, R. Wu, Y. Zeng, J. Wei, H. Li, L. Manna, A. D. Mohite, *Nanoscale* **2022**, *14*, 6743.
[20] X. He, Y. Deng, D. Ouyang, N. Zhang, J. Wang, A. A. Murthy, I. Spanopoulos, S. M. Islam, Q. Tu, G. Xing, Y. Li, V. P. Dravid, T. Zhai, *Chem. Rev.* **2023**, *123*, 1207.
[21] B. Zhang, Z. Xu, C. Ma, H. Li, Y. Liu, L. Gao, J. Zhang, J. You, S. Liu, *Adv. Funct. Mater.* **2022**, *32*, 2200174.
[22] Y. Zhang, Y. Liu, Z. Xu, Z. Yang, S. Liu, *Small* **2020**, *16*, 2003145.
[23] J. Cho, J. T. Dubose, A. N. T. Le, P. V. Kamat, *ACS Mater. Lett.* **2020**, *2*, 565.
[24] J. Zheng, Y. Zeng, J. Wang, C. Sun, B. Tang, Y. Wu, Y. Zhang, Y. Yi, N. Wang, Y. Zhao, S. Zhou, *J. Am. Chem. Soc.* **2021**, *143*, 21302.
[25] W. Shao, Q. Li, T. He, Y. Zhang, M. Niu, H. Wang, Z. Zhang, Y. Zhou, J. X. Wang, R. Fan, X. Xia, O. M. Bakr, O. F. Mohammed, H. Liang, *Adv. Funct. Mater.* **2023**, *33*, 2301767.
[26] M. Xia, Z. Xie, H. Wang, T. Jin, L. Liu, J. Kang, Z. Sang, X. Yan, B. Wu, H. Hu, J. Tang, G. Niu, *Adv. Mater.* **2023**, *35*, 2211769.
[27] P. Wan, T. Jin, R. Gao, X. Ouyang, Z. Feng, G. Niu, J. Tang, L. Liu, *Adv. Funct. Mater.* **2024**, *34*, 2308263.
[28] Y. Gao, P. Wan, T. Jin, H. Hu, L. Liu, G. Niu, *Small* **2023**, *19*, 2301530.
[29] W. Panaccione, Z. Shi, P. Kandlakunta, T. Nichols, S. White, J. Huang, L. R. Cao, *Nucl Instrum Methods Phys Res A* **2024**, *1064*, 169340.
[30] J. M. Gómez-Ros, R. Bedogni, C. Domingo, *Radiat. Meas.* **2023**, *161*, 106908.
[31] M. L. Litvak, I. G. Mitrofanov, I. O. Nuzhdin, A. V. Vostrukhin, D. V. Golovin, A. S. Kozyrev, A. V. Malakhov, M. I. Mokrousov, A. B. Sanin, V. I. Tretyakov, F. S. Fedosov, *Cosmic Research* **2017**, *55*, 110.
[32] M. Naito, H. Kusano, S. Kodaira, *Sci Rep.* **2023**, *13*, 13275.
[33] F. Tabbakh, N. S. Hosmane, *Sci Rep.* **2020**, *10*.
[34] M. El-Asery, Z. Sadoune, H. El Bekkouri, E. M. Al Ibrahmi, A. Didi, E. M. Chakir, *Springer Nature* **2023**, *78*, 810.
[35] F. Lédée, A. Ciavatti, M. Verdi, L. Basiricò, B. Fraboni, F. Lédée, A. Ciavatti, M. Verdi, L. Basiricò, B. Fraboni, *Adv. Opt. Mater.* **2022**, *10*, 2101145.
[36] J. Allison, K. Amako, J. Apostolakis, P. Arce, M. Asai, T. Aso, E. Bagli, A. Bagulya, S. Banerjee, G. Barrand, B. R. Beck, A. G. Bogdanov, D. Brandt, J. M. C. Brown, H. Burkhardt, P. Canal, D. Cano-Ott, S. Chauvie, K. Cho, G. A. P. Cirrone, G. Cooperman, M. A. Cortés-Giraldo, G. Cosmo, G. Cuttone, G. Depaola, L. Desorgher, X. Dong, A. Dotti, V. D. Elvira, G. Folger, et al., *Nucl Instrum Methods Phys Res A* **2016**, *835*, 186.
[37] S. Agostinelli, J. Allison, K. Amako, J. Apostolakis, H. Araujo, P. Arce, M. Asai, D. Axen, S. Banerjee, G. Barrand, F. Behner, L. Bellagamba, J. Boudreau, L. Broglia, A. Brunengo, H. Burkhardt, S. Chauvie, J. Chuma, R. Chytracek, G. Cooperman, G. Cosmo, P. Degtyarenko, A. Dell'Acqua, G. Depaola, D. Dietrich, R. Enami, A. Feliciello, C. Ferguson, H. Fesefeldt, G. Folger, et al., *Nucl Instrum Methods Phys Res A* **2003**, *506*, 250.
[38] J. Allison, K. Amako, J. Apostolakis, H. Araujo, P. A. Dubois, M. Asai, G. Barrand, R. Capra, S. Chauvie, R. Chytracek, G. A. P. Cirrone, G. Cooperman, G. Cosmo, G. Cuttone, G. G. Daquino, M. Donszelmann, M. Dressel, G. Folger, F. Foppiano, J. Generowicz, V. Grichine, S. Guatelli, P. Gumplinger, A. Heikkinen, I. Hrivnacova, A. Howard, S. Incerti, V. Ivanchenko, T. Johnson, F. Jones, et al., *IEEE Trans. Nucl. Sci.* **2006**, *53*, 270.
[39] D. B. Nicodkmus, H. H. Staubf, *Phys. Rev.* **1953**, *89*, 1288.
[40] S. Kasap, P. Capper, *Springer Handbook of Electronic and Photonic Materials*, 2nd ed., Springer, Cham, Switzerland, **2017**, https://doi.org/10.1007/978-3-319-48933-9.
[41] A. Selva, L. Bellan, P. Colautti, V. Conte, E. Fagotti, *LNL Annual Report* **2020**, 133.
[42] J. W. Meadows, *Nucl. Instrum. Methods Phys. Res. A.* **1993**, *324*, 239.
[43] T. L. Leung, I. Ahmad, A. A. Syed, A. M. C. Ng, J. Popović, A. B. Djurišić, *Commun. Mater.* **2022**, *3*, 63.
[44] A. R. Kirmani, T. A. Byers, Z. Ni, K. VanSant, D. K. Saini, R. Scheidt, X. Zheng, T. B. Kum, I. R. Sellers, L. McMillon-Brown, J. Huang, B. Rout, J. M. Luther, *Nat. Commun.* **2024**, *15*, 696.
[45] G. Konstantatos, J. Clifford, L. Levina, E. H. Sargent, *Nat. Photonics* **2007**, *1*, 531.
[46] G. Konstantatos, I. Howard, A. Fischer, S. Hoogland, J. Clifford, E. Klem, L. Levina, E. H. Sargent, *Nature* **2006**, *442*, 180.


© 2025 The Author(s). Advanced Functional Materials published by Wiley-VCH GmbH

16163028, 0, Downloaded from https://advanced.onlinelibrary.wiley.com/doi/10.1002/adfm.202502530 by Cambridge University Library, Wiley Online Library on [04/07/2025]. See the Terms and Conditions (https://onlinelibrary.wiley.com/terms-and-conditions) on Wiley Online Library for rules of use; OA articles are governed by the applicable Creative Commons License

[47] H. Fang, W. Hu, *Adv. Sci.* **2017**, *4*, 1700323.
[48] I. Fratelli, L. Basiricò, A. Ciavatti, L. Margotti, S. Cepić, M. Chiari, B. Fraboni, *Adv. Sci.* **2024**, *11*, 2401124.
[49] F. Liu, R. Wu, Y. Zeng, J. Wei, H. Li, L. Manna, A. D. Mohite, *Nanoscale* **2022**, *14*, 6743.
[50] J. H. Hubbell, S. M. Seltzer, *X-Ray Mass Attenuation Coefficients*, National Institute of Standards and Technology, Gaithersburg, MD **1995**, https://www.nist.gov/pml/x-ray-mass-attenuation-coefficients.
[51] M. J. Berger, J. S. Coursey, M. A. Zucker, J. Chang, *ESTAR, PSTAR, and ASTAR: Computer Programs for Calculating Stopping-Power and Range Tables for Electrons, Protons, and Helium Ions (version 1.2.3)*, National Institute of Standards and Technology, Gaithersburg, MD **2005**, https://physics.nist.gov/PhysRefData/Star/Text/ESTAR.html.
[52] Y. Lee, J. G. Kwak, Y. U. Nam, S. W. Yoon, H. S. Kim, G. Park, *Fusion Eng. Des.* **2020**, *153*.
[53] J. Qian, Y. Li, Y. Shen, X. Zhao, C. Wu, H. Gu, Z. Zhang, Y. Chen, B. Cai, J. Xia, W. Shen, K. Cao, L. Liu, L. Zhang, G. Cheng, S. Chen, G. Xing, W. Huang, *ACS Nano* **2024**, *18*, 15055.
[54] T. Zhang, C. Zhou, X. Feng, N. Dong, H. Chen, X. Chen, L. Zhang, J. Lin, J. Wang, *Nat. Commun.* **2022**, *13*, 60.
[55] B. Chen, R. Yu, G. Xing, Y. Wang, W. Wang, Y. Chen, X. Xu, Q. Zhao, *ACS Energy Lett.* **2024**, *9*, 226.
[56] D. Li, D. Li, A. Yang, H. Zhang, X. Lai, C. Liang, *ACS Omega* **2021**, *6*, 20877.
[57] R. Zheng, X. Gan, K. Li, S. Zhang, M. Xiang, L. Guo, H. Liu, *Opt Mater (Amst)* **2024**, *147*.
[58] A. Forde, S. Tretiak, A. J. Neukirch, *Nano Lett.* **2023**, *23*, 11586.
[59] Z. Fang, G. Wang, C. Guan, J. Zhang, Q. Xiang, *Angew. Chem., Int. Ed.* **2024**, *63*, 202411219.


© 2025 The Author(s). Advanced Functional Materials published by Wiley-VCH GmbH

16163028, 0, Downloaded from https://advanced.onlinelibrary.wiley.com/doi/10.1002/adfm.202502530 by Cambridge University Library, Wiley Online Library on [04/07/2025]. See the Terms and Conditions (https://onlinelibrary.wiley.com/terms-and-conditions) on Wiley Online Library for rules of use; OA articles are governed by the applicable Creative Commons License